

Chapter 5

Magnetic Properties of One-Dimensional Stacked Metal Complexes



Tabea Buban, Sarah Puhl, Peter Burger, Marc H. Prosenc
and Jürgen Heck

Abstract Cooperative effects such as ferro- or antiferromagnetic interactions are accessible through tailor-made molecular structures of linearly arranged paramagnetic complexes. Since it is well-known that subtle changes in the molecular structure can cause distinct changes in the magnetic interaction, the inter-metal distances were varied as well as the number of stacked complexes. In addition the metal centers were changed in order to vary the numbers of interacting unpaired electrons. The final target was an investigation of the properties of stacked magnetic molecules on a substrate.

5.1 Introduction

The study of molecular magnetic materials is an important issue in view of spintronic applications. In particular the following molecular materials were investigated and showed promising characteristics [1, 2]: Prussian Blue [3–5], spin-crossover systems [6, 7], tetracyanoethylene (TCNE) salts [8–10], single-molecular magnets [11–13] and single-chain magnets [14, 15]. Contributions to the research field of coupling mechanisms between paramagnetic sandwich compounds were made for various types of complexes [16]. Examples are metallocene and oligometallocene complexes [17, 18], decorated with a different number of unpaired electrons and which are directly linked [19–21] through a saturated [22, 23] or unsaturated [24, 25] bridge, or are part of a cyclophane entity [26–29].

T. Buban · S. Puhl · P. Burger (✉) · J. Heck
Institute of Inorganic and Applied Chemistry, University of Hamburg,
Martin-Luther-King-Platz 6, 20146 Hamburg, Germany
e-mail: burger@chemie.uni-hamburg.de

J. Heck
e-mail: heck@chemie.uni-hamburg.de

M. H. Prosenc
Institute of Physical Chemistry, TU Kaiserslautern, Erwin-Schrödinger-Str. 52,
67663 Kaiserslautern, Germany
e-mail: prosenc@chemie.uni-kl.de

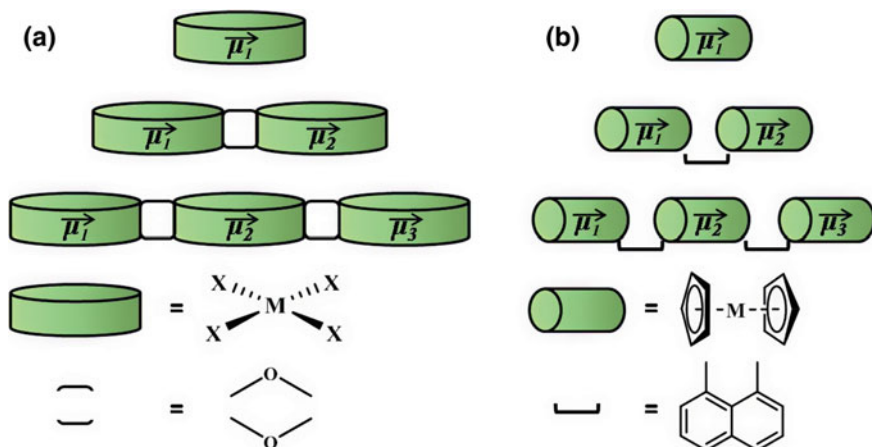


Fig. 5.1 Stacking of paramagnetic complexes **a** salen, salenophen, pyridine-diimine complexes and **b** metallocenes; $\vec{\mu}_i$: magnetic moment of the subunit

Spin filters and spin-based logic devices open the door to exciting new applications and are based on magnetic rather than electric interactions. Currently, such logic devices are realized with individually arranged atoms on surfaces and require low temperatures due to their small magnetic coupling [30]. Here molecules come into play, which allow to access significantly larger magnetic interactions of the spin centers. Furthermore, they offer the opportunity to adjust the size and sign, i.e. antiferro- versus ferromagnetic coupling by tailor-made design of synthetic structures. In this regard one-dimensional stacked complexes are promising candidates [31–33]. We investigated two different types of paramagnetic 3d transition metal systems, which will be discussed in separate sections. In the first part of this chapter, paramagnetic Schiff-base complexes with salene and pyridine-diimine (PDI) ligands are discussed, in which the metal centers are placed in the plane of the ligand's π -bonds (Fig. 5.1a). A particular focus is placed on the magnetic coupling pathways of the individual molecules and in the bulk, in solution as well as in the solid state. Their surface deposition, orientation and magnetic interaction, e.g. surface-mediated Ruderman–Kittel–Kasuya–Yoshida (RKKY) coupling, will also be discussed. In the second section, di-, tri- and tetranuclear cofacially stacked sandwich complexes are reported, in which the metal centers are located perpendicular to the π -plane of the ligand (Fig. 5.1b).

5.2 Towards Molecular Spintronics

Recent advances in atom manipulation led to structures and devices suitable for storage and processing of spin information [34]. However, these structures require single atom manipulation techniques as well as very low temperatures.

If laterally linked molecular complexes were used, they need to be robust, paramagnetic and depositable on a surface. With this goal in mind, we screened suitable complexes and ligand strategies [35, 36]. While molecular cobalt salen complexes appear to be mobile on a Cu(111) surface, chlorinated derivatives arrange via self-assembly forming small six-membered aggregates to extended domains on surfaces (Fig. 5.2c).

Deposition of salen complexes on Cu yielded slightly mobile complexes for salen and methylsalen derivatives. Thus, further studies were performed using salophen complexes with a phenylendiamine bridge, which was deemed to yield more rigid complexes.

Deposition of dibromo salophen complexes on Au(111) revealed more stable complexes, which arrange in four-membered aggregates forming long bands on Au(111) (Fig. 5.3). Upon heating they initially loose bromine atoms and convert to small to long chemically bonded chains by C–C bond formation (Fig. 5.4) [37]. The lengths of the chains can be controlled by surface occupancy and temperature [38]. If in addi-

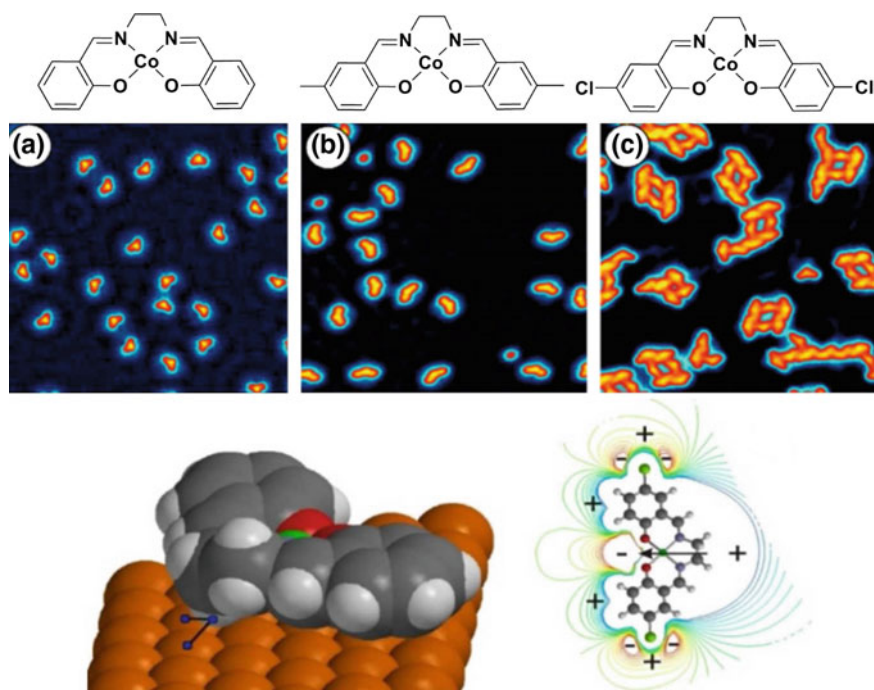


Fig. 5.2 Cobalt salen complexes on a Cu(111) surface. **a** cobalt salen, **b** 4,4' dimethyl cobalt salen and **c** 4,4 dichloro cobalt salen complexes. For all complexes 12 orientations were found representing the six-fold symmetry of the surface together with the delta and lambda configuration. On the bottom one optimized structure of the cobalt salen complex is depicted exhibiting weak CH...Cu interactions. Calculation of the charge distribution resulted in the accumulation of negative charges on the salen oxygen atoms while the α - and β -hydrogen atoms exhibit positive charges important for self-assembly of the chloro complexes

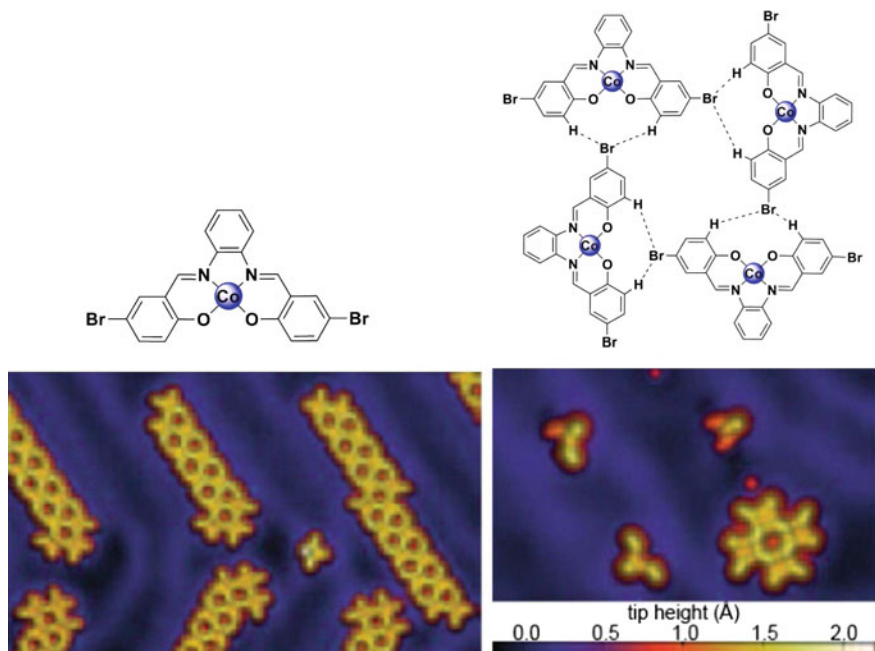


Fig. 5.3 Dibromo salophen cobalt complex (upper left), self assembled to form four-membered rings (upper right), and their observation on Au(111) surfaces by STM techniques [37] (bottom)

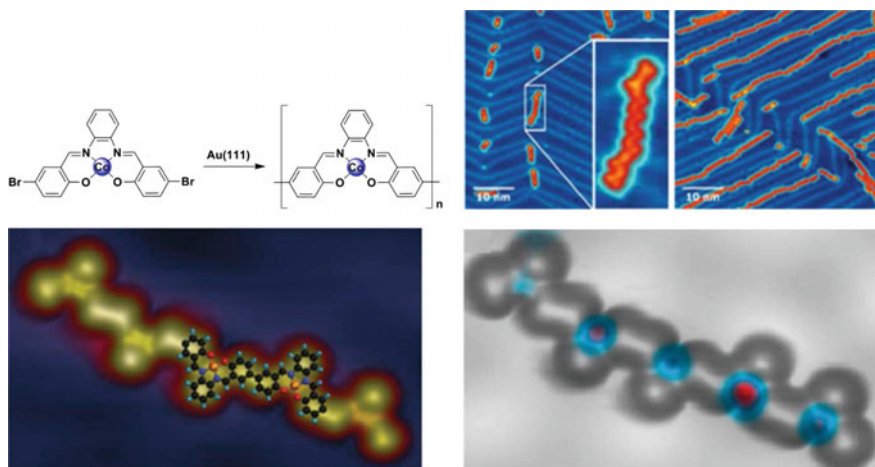
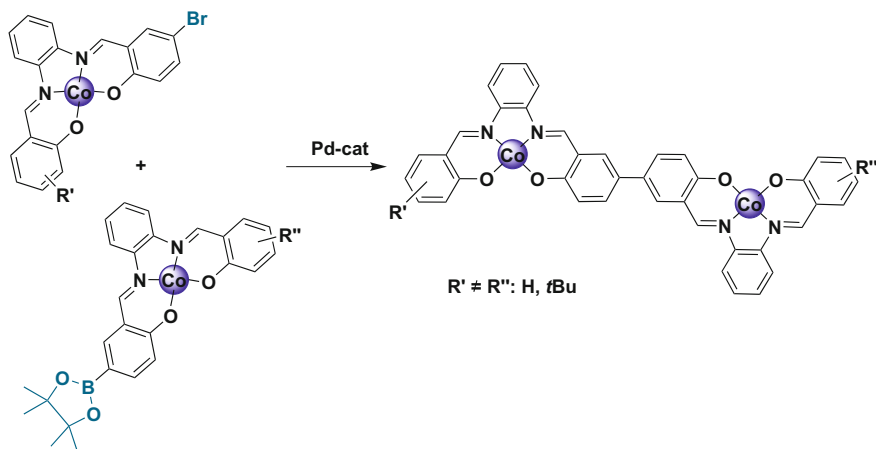


Fig. 5.4 On surface oligomerization of dibromo cobalt salophen. Small to long chains can be achieved depending on the amount of the monobromo cobalt salophen, which terminates the chains (top). On the bottom one selected chain and Kondo-measurements revealing the antiferromagnetic structure are depicted



Scheme 5.1 Synthesis of disalophen complexes according to [39]

tion monobromo salophen complexes were deposited, more defined chains formed up to about 100+ Co-salophen units [38]. These cobalt complex chains consist of chemically connected paramagnetic Co(II) complexes. This raises the question about the strength and type of magnetic coupling between the Co(II) centers.

Kondo measurements of the cobalt salophen chains on surfaces revealed a dependency of the Kondo temperature on the parity of the chain length and consequently an antiferromagnetic coupling among the metal centers [37]. In order to obtain information about the magnetic coupling in the bulk material, we synthesized dicobalt- and dicopper-disalophen complexes (Scheme 5.1) and investigated their magnetic properties [39, 40].

Magnetic measurements by the SQUID-methods revealed strong (Co) and weak (Cu) antiferromagnetic couplings between the metal centers [39, 40]. These results are in agreement with measurements of the magnetic properties of the chains deposited on Au(111) surfaces [37].

From X-ray crystal structure data as well as density function theory (DFT) calculations, the rotation angle around the central C–C bond linking the two salophen units is close to 0°. DFT calculations of the spin density of a dicobalt complex revealed that the two unpaired electrons are distributed in the π -electron system of the complex (Fig. 5.5). A rotation around the central C–C bond would reduce the overlap between the orbitals at the bridgehead carbon atoms and thus the coupling between the unpaired electrons at the metal spin centers.

A maximum magnitude of J was found in a coplanar arrangement, which was also found for Co-salophen complexes deposited on Au(111) [37–39, 41, 42]. From XAS-, STM-measurements and DFT calculations it became evident that the coupling between the complexes on the surface is dominated by the coupling between the the Co(II) spin centers through the ligand's π -system rather than surface mediated by RKKY interactions. The observed antiferromagnetic coupling together with the

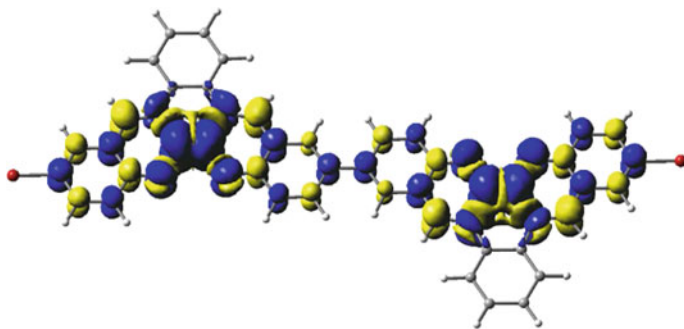


Fig. 5.5 DFT calculated spin-density of a dibromo dicobalt salophen complex. The spin density is located in π -orbitals perpendicular to the molecular plane

formation of long one-dimensional chains raises the question whether these systems could be employed in spintronic devices [41].

A simple spintronic device could be a logic gate, which transfers the information from two leads to an exit gate [41]. To build such a device, we synthesized a tri-cobalt-triplesalophen complex [41, 43] with three bromine atom substituents to be copolymerized with mono- and dibromocobaltsalophen complexes on a metal surface [38, 41]. Such a spintronic device is depicted in Fig. 5.6.

In conclusion, we were able to develop new spin devices from salophen complexes. Initial studies on salen complexes revealed the high thermal and chemical stability of cobalt complexes on Cu(111) and Au(111) surfaces. Self-assembly of halogen terminated complexes and further chemical transformation of the bromo derivative into complex chains with antiferromagnetically coupled unpaired electrons revealed the first molecular based spin-chains on metal surfaces with high Kondo temperatures depending on the chain length. Triple-cobaltsalophen complexes were used in addition to mono- and dibromosalophen cobalt complexes and resulted in structures suitable for a model of a molecular based spintronic device.

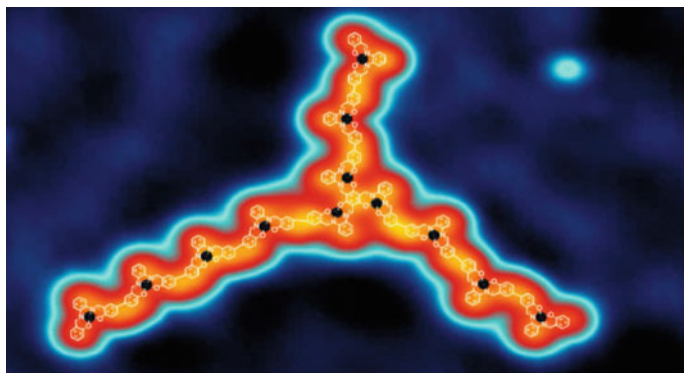


Fig. 5.6 STM-representation of the synthesized spintronic device. The central triple-cobaltsalophen complex is chemically connected to cobalt salophen complex-chains

5.3 Paramagnetic 3d-Transition-Metal Complexes with Terdentate Pyridine-Diimine Ligands

Pyridine-Diimine (PDI) ligands are classified as non-innocent” ligands whose complexes can feature interesting electronic and magnetic properties [44–48]. Spacer-connected PDI ligands provide access to dinuclear complexes with adjustable metal-metal distances (Fig. 5.7).

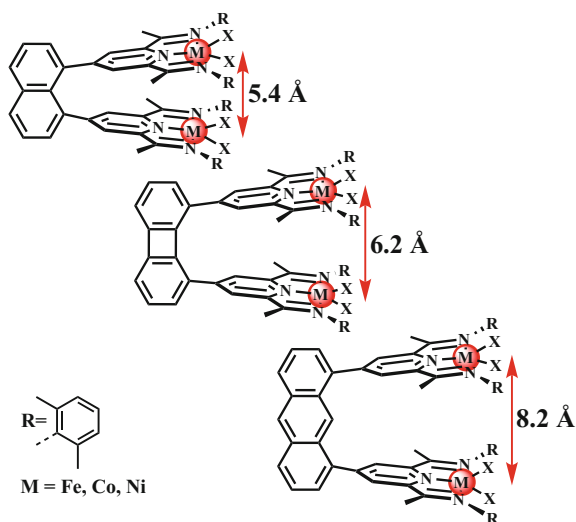
Due to the perpendicular alignment of the planes of the PDI systems and the bonded aromatic spacer, a magnetic coupling of the metal centers via super-exchange is likely to be prevented. DFT-calculated spin densities of the anthracenyl-bridged complex support this assumption [49]. It was therefore anticipated that the systems presented in Fig. 5.7 would allow the investigation of the dependence of the dipolar coupling on the metal-metal distances.

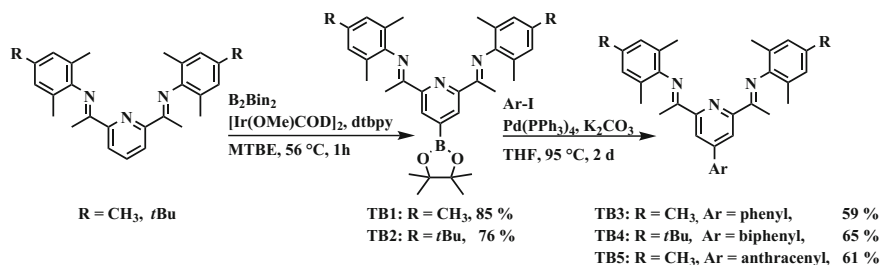
5.3.1 Synthesis of Novel Mono-, Di- and Trinuclear Iron(II) Complexes

The key building blocks for the desired novel ligand systems are the borylated pyridine-diimine precursors **TB1** and **TB2**. These compounds were obtained by direct regioselective borylation with an iridium catalyst and were subjected to a consecutive Suzuki–Miyaura [50, 51] cross-coupling reaction (Scheme 5.2).

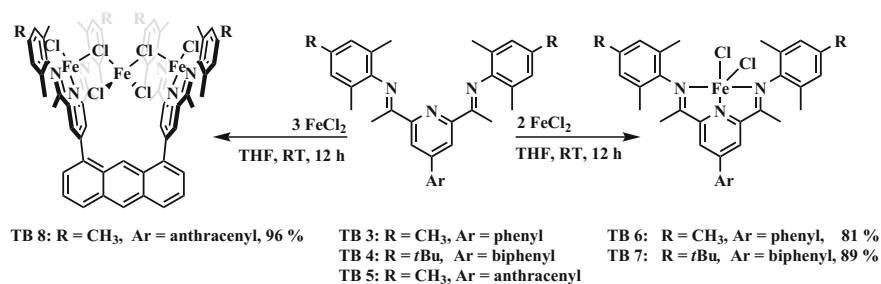
Complexation to the iron(II)-compounds was successfully accomplished using a synthetic protocol of Campora et al. (Scheme 5.3) [52]. For ligands **TB3** and **TB4**

Fig. 5.7 Novel complexes with different metal-metal distances





Scheme 5.2 Synthesis of ligands **TB5–TB7**



Scheme 5.3 Complexation of FeCl₂ by ligands **TB3**, **TB4** and **TB5** to form mono-, di- and trinuclear complexes

the reaction led to the expected mono- and dinuclear complexes **TB6** and **TB7**. In the case of the ligand **TB5**, a trinuclear complex with a bridging FeCl₂-group was obtained.

The molecular structures of the iron(II) complexes (Fig. 5.8) could be unambiguously established through X-ray crystal structure analyses. Selected bond distances and angles are listed in Table 5.1. In all complexes the iron atoms exhibit a slightly distorted square-pyramidal geometry with values for Addison's parameter $\tau_5 \leq 0.15$. The Fe–Cl bond length is in the typical range of 2.25–2.28 Å for iron(II) complexes [53, 54]. The observed bond distances and angles of the PDI ligand compare well with structural data in the literature [55–57]. The C–N and C–C distances of the diimine groups and the exocyclic C–C bonds of the pyridine group clearly speak in favour of a neutral, i.e. innocent pyridine-diimine ligand [48, 58, 59]. The observed inter-metal distance of the dinuclear compound (Fe1–Fe2 = 7.235 Å) is larger than the DFT derived value (6.2 Å), whereas the distance in the trinuclear complex (Fe1–Fe3 = 7.804 Å) differs slightly from the calculated distance of a related dinuclear complex (8.2 Å), due to the interlinked iron(II) chlorido group.

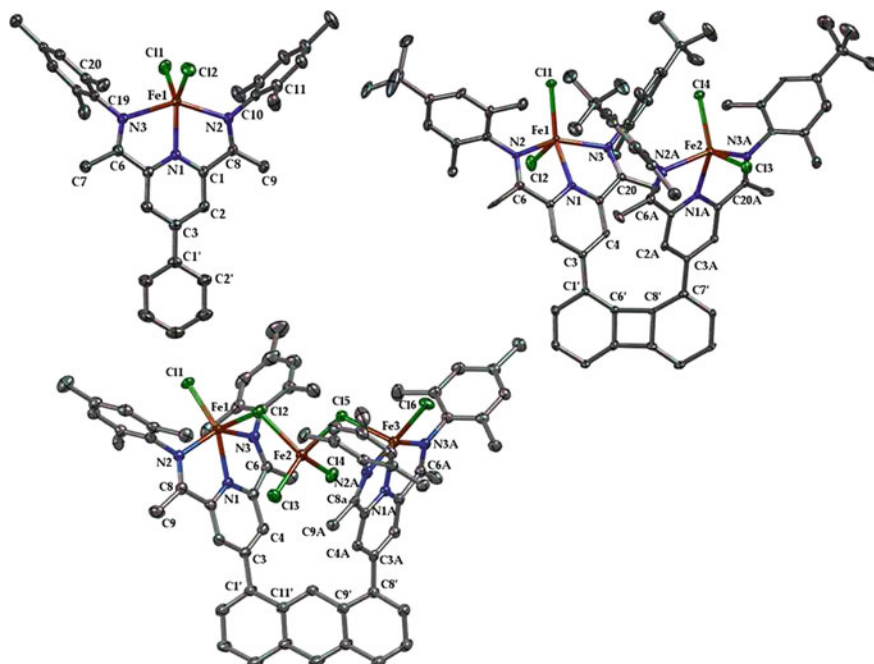


Fig. 5.8 X-ray crystal structures of **TB6–TB8**; co-crystallized solvent molecules and hydrogen atoms are partially omitted for clarity

Table 5.1 Selected distances (Å) and angles (°) for **TB6**, **TB7** and **TB8** with estimated standard deviation (esd) in parentheses

	TB6	TB7	TB8
Fe1–Cl1	2.2882(11)	2.270(2)	2.2513(1)
Fe1–Cl2	2.2876(10)	2.310(3)	2.3943(1)
Fe1–N1	2.103(3)	2.099(7)	2.110(3)
Fe1–N2	2.272(3)	2.258(7)	2.221(3)
Fe1–N3	2.254(3)	2.229(7)	2.195(3)
N3–C6	1.280(5)	1.295(11)	1.288(5)
N2–C8	1.284(4)	1.276(11)	1.279(5)
C1–C8	1.494(5)	1.498(11)	1.479(6)
C5–C6	1.491(5)	1.497(11)	1.485(6)
N2–Fe1–N3	145.40(10)	73.3(2)	144.60(1)
N1–Fe1–Cl1	125.39(9)	148.6(2)	149.45(9)
N1–Fe1–Cl2	125.80(9)	95.9(2)	101.70(9)

5.3.2 Electronic and Magnetic Properties

First insight into the magnetic properties was obtained by variable temperature ^1H NMR measurements. In the accessible temperature range of 225–300 K, only the trinuclear compound **TB8** shows Curie behavior (Fig. 5.9). While the ^1H NMR resonances of the mono- and dinuclear complexes display a linear dependence on the reciprocal temperature, the corresponding intercepts deviate significantly from zero.

This is particularly pronounced for the mononuclear complex **TB6** and might be attributed to large zero field splitting (ZFS) parameters and/or low-lying excited states mixed into the ground state. For iron PDI complexes magnetic moments ranging from $\mu_{\text{eff}} = 5.0 \mu_{\text{B}}$ to $5.8 \mu_{\text{B}}$ and ZFS parameters in the range from $D = -10$ – 20 cm^{-1} with d^6 -configured iron centers with a $S = 2$ spin state were previously reported in the literature [52, 60, 61].

To establish the electronic ground (and potential excited) states of the iron complexes, Mössbauer spectroscopy was employed for the novel complex **TB6** (Fig. 5.10). The derived parameters are listed in Table 5.2. At 80 K, the spectrum displays the expected doublet as reported in the literature [48, 62] with an isomeric

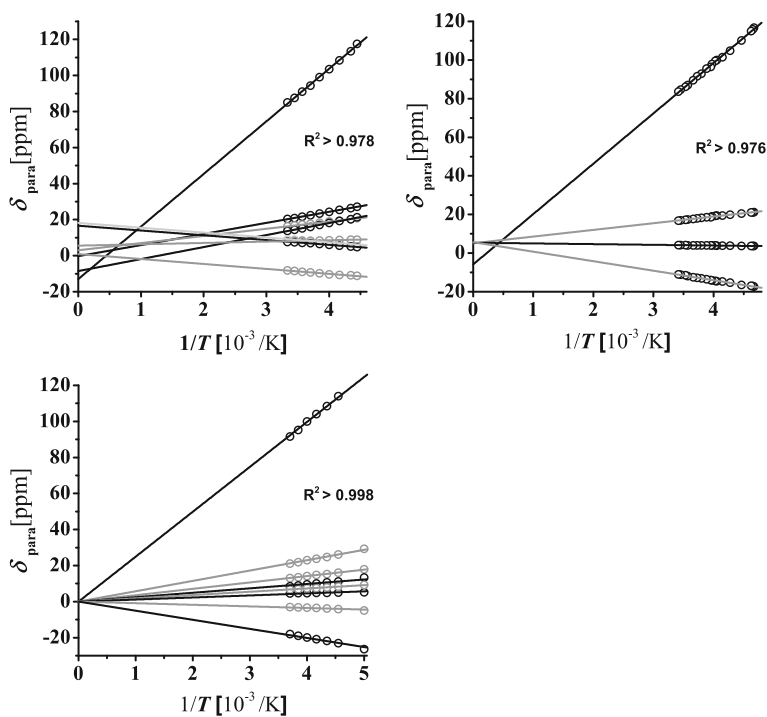


Fig. 5.9 ^1H NMR shifts from **TB8** (left), **TB9** (middle) and **TB10** (right)

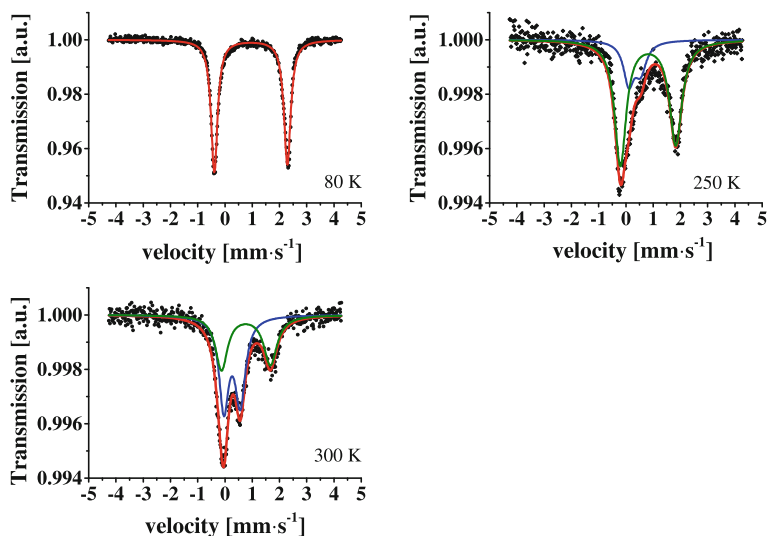


Fig. 5.10 Mössbauer spectra of complex **TB6** at 80, 250, and 300 K

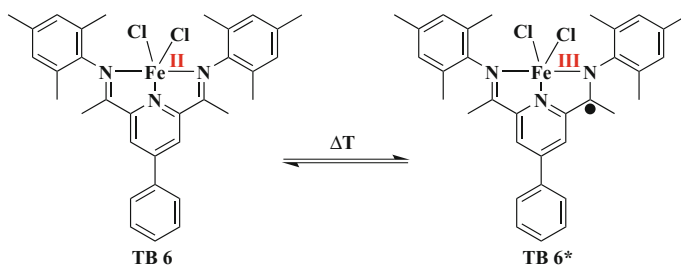
Table 5.2 Parameters of the Mössbauer spectra at different temperatures

T (K)	δ_{IS} (mms^{-1})	ΔE_{Q} (mms^{-1})	Assignment	Population (%)
80	1.06	2.68	Fe(II)	100
250	0.92	2.03	Fe(II)	80.3
250	0.43	0.44	Fe(III)	19.7
300	0.88	1.80	Fe(II)	52.8
300	0.17	0.60	Fe(III)	47.2

shift of $\delta_{\text{IS}} = 1.06 \text{ mms}^{-1}$ and a quadrupole splitting of $\Delta E_{\text{Q}} = 2.68 \text{ mms}^{-1}$ typical for high-spin iron(II) center with $S = 2$ [63, 64].

With increasing temperature, a second doublet emerges, indicating two different states of the complex. The isomeric shift of $\delta_{\text{IS}} = 0.037 \text{ mms}^{-1}$ of the second doublet is typical for d^5 -configured iron high-spin complexes [62], while the quadrupole splitting value of $\Delta E_{\text{Q}} = 2.68 \text{ mms}^{-1}$ is significantly smaller than values previously reported for real iron(III) PDI-complexes [62]. The quadrupole splitting of the aforementioned quintet decays at higher temperatures indicating a small change of the coordination geometry [65]. The observed temperature dependence of the isomeric shift is not consistent with the expected influence of a second-order Doppler effect [66] and is instead accounted for by dynamic processes between the two states.

Iron(II) PDI complexes with a reduced, i.e. non-innocent ligand are known to exhibit smaller quadrupole splittings [48]. Therefore, it is suggested that at higher temperatures an iron(III) complex bearing an anionic non-innocent ligand is populated. This indicates a case of valence tautomerism as shown in Scheme 5.4 [67].



Scheme 5.4 Assumed temperature dependent valence tautomerism in complex **TB6**

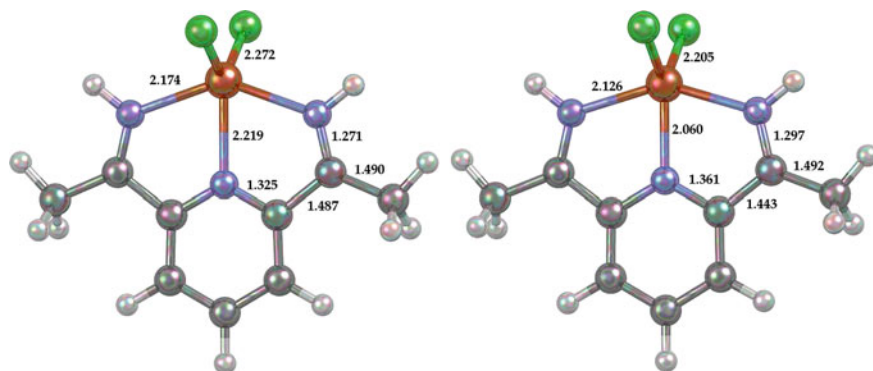


Fig. 5.11 Calculated molecular structures of Fe(II)-complex (left) and Fe(III)-complex (right) with selected bond-distances in Å

Starting from our DFT calculations, Granovsky carried out multi-reference calculations for both iron(II) and iron(III) centers with $S = 2$ and $S = 3$ spin states at the XMCQDPT2/SAS-CASSCF [13e, 11o] level [68] for the model system shown in Fig. 5.11. The energy difference between the $S = 2$ ground state and the $S = 3$ excited state is calculated to be $\Delta E = 7.3 \text{ kcal mol}^{-1}$. Preliminary results for calculations with larger basis sets and the full ligand system suggest that the energy difference is even smaller for the substituted real complex. Therefore, it is anticipated that the $S = 3$ excited state is populated to a significant extent above 300 K.

The calculations predicted an alteration in the bond length of the ligand, i.e. the C–N distances of the imine groups are elongated by 0.03 \AA and the exocyclic C–C bonds of the pyridine group is shortened by 0.04 \AA . These theoretically derived changes are smaller than for reported non-innocent” PDI ligands [58]. It was therefore not surprising that we were not able to detect changes in the bond lengths in temperature dependent single crystal structure measurements.

Figure 5.12 displays the temperature dependence of the effective magnetic moment μ_{eff} for compounds **TB6**, **TB7** and **TB8**. The results of the Curie–Weiss analysis and fitting parameters of the variable temperature (vt) magnetic susceptibility data obtained with the JulX [69] program are given in Table 5.3. For all three complexes

Fig. 5.12 Plot of μ_{eff} versus T for **TB6** (bottom), **TB7** (middle) and **TB8** (top)

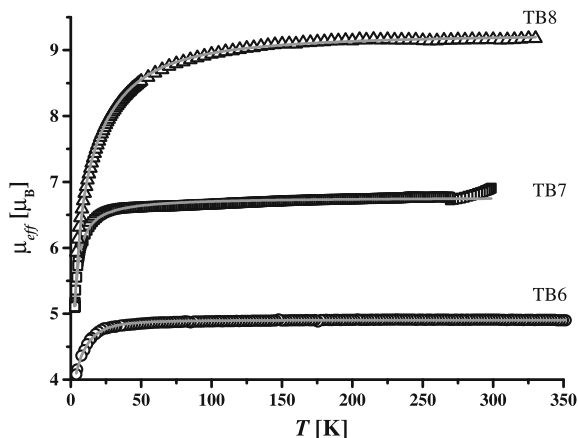


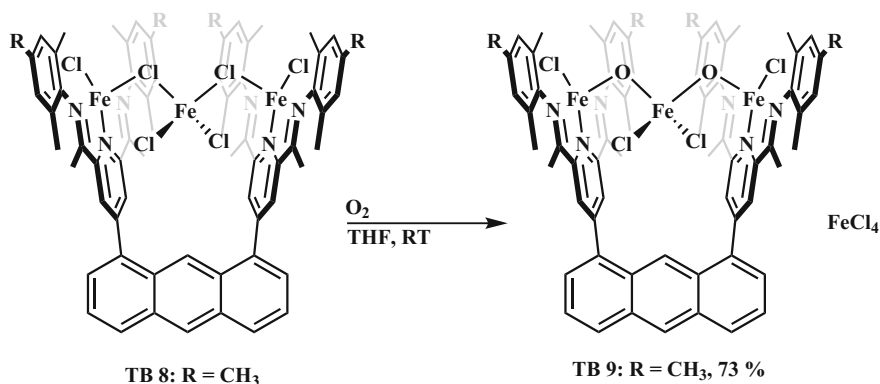
Table 5.3 Parameters obtained from fitting the magnetic data of **TB6**, **TB7** and **TB8**

Compound	S	g -Value	D (cm^{-1})	J (cm^{-1})	Θ_{W} (K)	μ_{eff} (μ_{B})
TB6	2	2.052	-8.414	-	1.400	4.90
TB7	2	1.954	-0.209	0.001	-1.949	6.77
TB8	2	2.180	-24.435	-0.390	7.98	9.17

the magnetic moment increases with higher temperatures until it reaches saturation at 70 K for **TB6**, 27 K for **TB7** and 140 K for **TB8**.

The magnetic moment of $\mu_{\text{eff}} = 4.9 \mu_{\text{B}}$ for the mononuclear complex **TB6** at RT is in the range for iron(II) high-spin complexes and corresponds to the calculated spin-only value. For systems displaying valence tautomerism, a change of the magnetic moment is typically observed above 250 K [70–72]. This was, however, not observed for compound **TB6** and may be attributed to strong antiferromagnetic coupling between the iron $S = 3$ centre and the ligand radical. This could quench the additional magnetic moment as was previously reported for an iron complex by Banerjee et al. [73]. Simulations proposed a strong coupling constant of $J \approx -250 \text{ cm}^{-1}$ thus preserving the magnetic moment.

The determined ZFS parameter of $D = -8.4 \text{ cm}^{-1}$ matches the established values reported in the literature for related PDI iron complexes [62]. At room temperature a magnetic moment of $\mu_{\text{eff}} = 6.77 \mu_{\text{B}}$ is observed for the dinuclear complex **TB7**. This value indicates an uncoupled system with a $S = 2$ ground state for the independent iron centres and is in full agreement with the theoretical value of $\mu_{\text{theo}} = 6.93 \mu_{\text{B}}$. This is consistent with the fit of the magnetic susceptibility data, which revealed a negligible antiferromagnetic coupling between the iron centers ($J = -0.001 \text{ cm}^{-1}$). The ZFS parameter ($D = -0.209 \text{ cm}^{-1}$) is exceptionally small compared to the mononuclear compounds and could not be explained up to now. The magnetic moment of $\mu_{\text{eff}} = 9.17 \mu_{\text{B}}$ for the trinuclear compound **TB8** is comparable to the spin-only value for an uncoupled system containing three



Scheme 5.5 Reaction to oxo-complex **TB9** from **TB8**

high-spin iron(II) centers ($\mu_{\text{theo}} = 8.40 \mu_{\text{B}}^1$). For the data fit a spin state of $S_1 = S_2 = S_3 = 2$ was assumed in agreement with the Mössbauer measurements. Based on symmetry arguments, equal parameters were assigned to the outer iron atoms. The derived ZFS parameter of $D = -48.0 \text{ cm}^{-1}$ compares well with the expected value of (ideal) square-pyramidal coordination geometry ($\tau_5 = 0.08$) [77]. The fit also shows an antiferromagnetic coupling between the outer and inner metal centres by super-exchange via the μ -chlorido bridges.

5.3.3 Molecules on Surfaces

The MALDI mass spectra of the di- and trinuclear complexes display only peaks for the mononuclear fragments with $m/z = 599.1$ for **TB6**, $m/z = 1238.7$ for **TB7** and $m/z = 1059.45$ for **TB8**. Complex **TB8** was also examined via ESI mass spectrometry to check its accessibility for electro-spray deposition on surfaces. Rather than the expected mother iron peak, however, the recorded spectra and the isotropic pattern of the observed signal at $m/z = 1311.22$ hinted at an oxidized fragment.

The control reaction of compound **TB8** with oxygen led indeed and instantaneously to the μ -oxo-bridged iron(III) cationic complex **TB9** (Scheme 5.5), which was unambiguously confirmed by X-ray single crystal structure analysis. The spin state of $S = 5/2$ for all three iron centres could be established by Mössbauer spectroscopy.

Due to its inherent stability, the oxidized complex **TB9** was deposited on a Au(111)-surface by the electro-spray-deposition method [41, 78, 79]. Figure 5.13 shows topographical images of the measurements. Based on the crystal structure an intact molecule possesses a diameter of 1 nm. Most of the observed conformations

¹Calculated with $\mu_{\text{M}}^2 = \sum \mu_i^2$ [74–76].

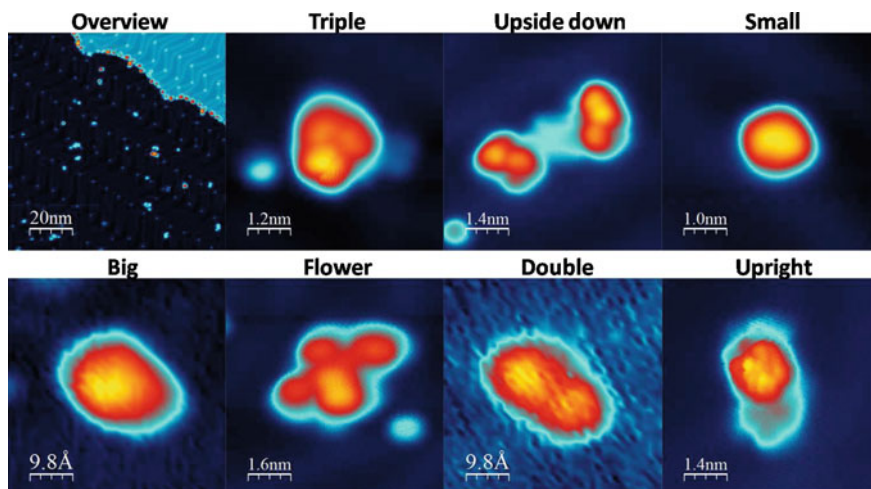


Fig. 5.13 Scanning tunnelling microscope images of the molecules deposited onto a Au(111) surface

are not robust and exist in many variants on the surface. Many of the objects agglomerate into pairs or trimers adsorbed at the elbows of the herringbone reconstruction of the Au(111) surface.

Theoretical calculations to determine the favored orientation of the molecules on the surface were performed by Hermanowicz [80] with the SIESTA DFT program package employing the PBE functional. These calculations revealed an energetic preference for the side-on orientation of 121 kcal/mol over the upside-down orientation (Fig. 5.14).

The STM measurements clearly revealed that the molecule lands in all possible rotational orientations on the surface. Similar results were obtained for a Fe_4 complex by Burgess [81], where an assignment of the DFT calculated structure to a topographical image was possible due to characteristic spin excitation energies. In our case a comparison of the measured topography images to the ones predicted by DFT calculations was not yet possible.

5.4 One-Dimensional Stacked Metallocenes

One final target was to stack paramagnetic metallocenes head-to-head and fix them in *peri*-position of a naphthalene unit. Herein, we present the synthesis, molecular structure, magnetic properties and theoretical calculations of bis- and oligo(metallocenyl)naphthalene complexes displaying different ground states.

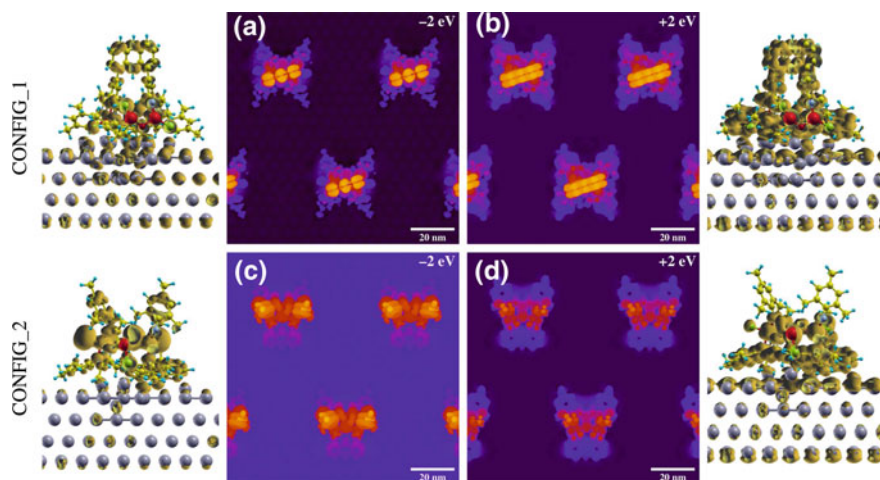


Fig. 5.14 Calculated maps as Tersoff–Hamann [82] style STM images (a–d) with corresponding 3D distributions (side views). Side on and upside orientation

5.4.1 Different Metal Centers

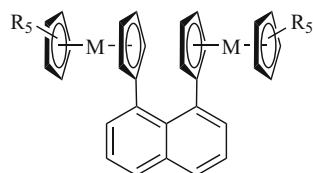
Depending on the metal used, the number of unpaired electrons per metallocenyl unit is predefined. Therefore the synthesized naphthalene-bridged biscobaltocenyl complex $[\text{Co}]_2$ [83], the bisvanadocenyl complex $[\text{V}]_2$ [84] as well as the decamethyl biscobaltocenyl $[\text{Co}^*]_2$ [83] and bisnickelocenyl compounds $[\text{Ni}^*]_2$ [85] (Fig. 5.15) exhibit different ground states. As a consequence, different magnetic responses should be expected by the combination of different metals.

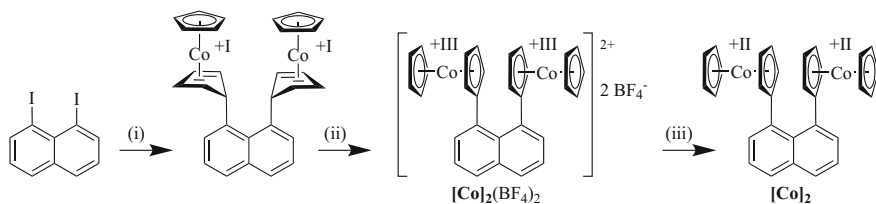
Synthesis

The dinuclear cobaltocene complex $[\text{Co}]_2$ was prepared in a three-step synthesis (Scheme 5.6) using 1,8-diiodonaphthalene as starting material [86]. A two-fold iodine-lithium exchange followed by a nucleophilic attack at cobaltocenium iodide led to a naphthalene-bridged dinuclear cobalt(I) complex. Hydride abstraction using a tritylium salt yielded the dinuclear cobaltocenium complex, which was readily reduced to the desired biscobaltocenyl complex using decamethylcobaltocene [83].

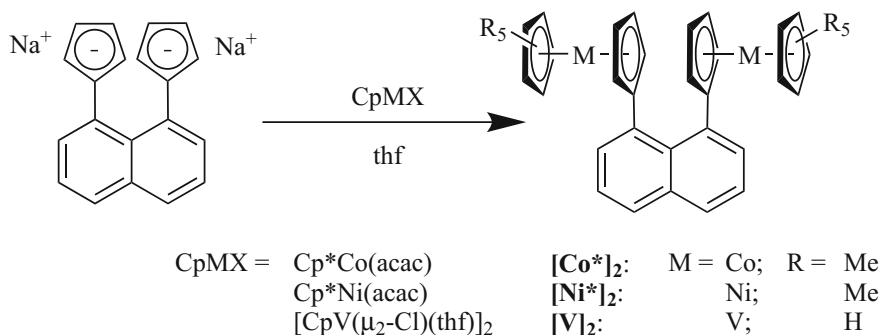
For the synthesis of the corresponding decamethyl biscobaltocenyl complex $[\text{Co}^*]_2$ [83] the disodium salt of a cyclopentadienyl functionalized naphthalene

Fig. 5.15 Naphthalene-bridged bismetallocenyl complexes $[\text{M}]_2$ ($\text{M} = \text{Co}$, V ; $\text{R} = \text{H}$) and $[\text{M}^*]_2$ ($\text{M} = \text{Co}$, Ni ; $\text{R} = \text{Me}$)





Scheme 5.6 Synthesis of the naphthalene-bridged biscobaltocenyl complex $[\text{Co}]_2$ [83, 86]; reaction conditions: (i): (1) $n\text{-BuLi}$, Et_2O , (2) $[\text{CoCp}_2]\text{I}$, Et_2O ; (ii): $\text{Ph}_3\text{C}^+\text{BF}_4^-$, dichloromethane (dcm); (iii): Cp^*_2Co , tetrahydrofuran (thf)



Scheme 5.7 Synthesis of the naphthalene-bridged bismetallocenyl complexes $[\text{Co}^*]_2$ [83], $[\text{Ni}^*]_2$ [85] and $[\text{V}]_2$ [84]

was used as starting material (Scheme 5.7). Reaction with a Cp^*Co transfer reagent yielded the desired dinuclear compound via salt metathesis. In analogous manner, the related decamethyl nickel complex $[\text{Ni}^*]_2$ [85] and the bisvanadocenyl complex $[\text{V}]_2$ [84] were accessible.

Molecular Structures

The molecular structures of the naphthalene-bridged bismetallocenyl complexes (Fig. 5.16) are dominated by a distortion (Table 5.4) due to the steric demand of the two metallocenyl entities in the *peri*-positions of the naphthalene linker.

The repulsion of the metallocenyl substituents is reflected in the angle between the linked cyclopentadienyl (Cp) ligands ($\angle\text{Cp-Cp}$) and the torsional angle (Fig. 5.17). The rotational angle of the adjacent Cp ring and the corresponding six-membered subunit of the naphthalene linker ($\angle\text{Cp-Ar}$) displays a deviation from the expected ideal head-to-head arrangement of the metallocenes. This might strongly influence the coupling pathway [83–85] that is either through space and/or through bond.

Table 5.4 Selected distances [Å] and angles [°] determined by X-ray crystal structure analysis of [Co]₂ [83], [Co*]₂ [83], [Ni*]₂ [85] and [V]₂ [84] with esd

	[Co] ₂	[Co*] ₂	[Ni*] ₂	[V] ₂
M1–M2	6.7392(4)	6.7244(7)	6.9705(3)	7.1212(3)
<i>ipso–ipso</i>	2.940(2)	3.018(4)	2.987(2)	2.974(1)
<i>peri–peri</i>	2.559(2)	2.563(5)	2.562(3)	2.565(1)
torsion [†]	29.7(1)	36.8(2)	27.6(1)	27.19(8)
∠Cp–Cp	28.46(6)	33.7(1)	31.48(7)	26.68(4)
∠Cp–Ar	40.28(5)	28.0(1)	42.40(6)	47.93(4)

[†]For the definition of the angle between the best-fit planes [87] of the corresponding atoms (∠) and the torsional angle see Fig. 5.17

Magnetic Properties

The magnetic behavior of the bimetallocenyl complexes in solution was studied by temperature dependent ¹H NMR spectroscopy. All naphthalene-bridged bimetallocenyl complexes displayed Curie behavior in the observed temperature range [83–85]. However, unusual diamagnetic chemical shifts δ_{dia} were obtained from a linear fit of the experimental chemical shift (5.1) possibly indicating small exchange interactions.

In the solid state all compounds displayed antiferromagnetic behavior. The simulation [69] of the magnetic data revealed a strong influence of the metal center on the exchange interaction between the two spin centers (Table 5.5). While for [Co]₂ [83] and [Ni*]₂ [85] similar weak antiferromagnetic exchange interactions were determined (-28.1 and -31.5 cm⁻¹) only a very weak coupling was found for [Co*]₂ [83] and [V]₂ [84]. While the decreased interaction in [Co*]₂ compared to [Co]₂ was attributed to geometric changes of the complexes in the solid state [83], the very weak interaction in [V]₂ can be attributed to electronic effects [84]. In cobaltocene and

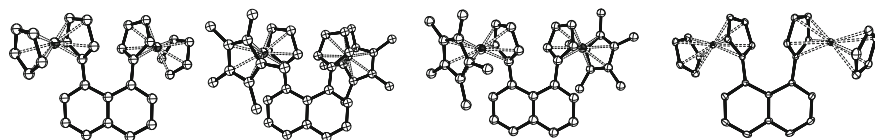
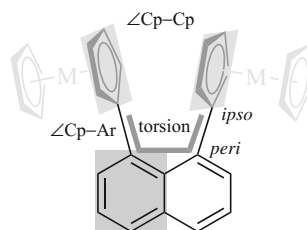
**Fig. 5.16** Molecular structures of [Co]₂ [83], [Co*]₂ [83], [Ni*]₂ [85] and [V]₂ [84] (left to right); hydrogen atoms are omitted for clarity**Fig. 5.17** Schematic representation of the molecular structure of [M]₂

Table 5.5 Experimental and calculated DFT parameters obtained from fitting of the magnetic data of $[\text{Co}]_2$ [83, 88], $[\text{Co}^*]_2$ [83], $[\text{Ni}^*]_2$ [85] and $[\text{V}]_2$ [84] in the solid state using the Heisenberg model $\hat{\mathcal{H}} = -2J_{12}S_1S_2$ and coupling constants calculated with the TPSSH functional (def2-TZVP basis set)

	$[\text{Co}]_2$	$[\text{Co}^*]_2$	$[\text{Ni}^*]_2$	$[\text{V}]_2$
$S_1 = S_2$	1/2	1/2	1	3/2
J_{12} (cm^{-1}) (DFT)	-28.1	-5.9	-31.5	-2.00 (-0.5 [†] -0.4 [‡])
$g_1 = g_2$	1.85	2.04	1.81	1.96
Θ_W (K)	-1.6	-4.9	1.40	-3.94
T_N (K)	≈ 48	≈ 4	≈ 101	≈ 8
$D_1 = D_2$ (cm^{-1})	-	-	n/a	2.83
μ_{eff} (B) (300 K)	2.15	2.47	3.20	5.28 (270 K)

[†]Obtained from the Greens-function approach [89, 90]; [‡]obtained from the broken-symmetry approach [91]; Θ_W : Weiss constant; T_N : Néel temperature; D : zero-field splitting parameter

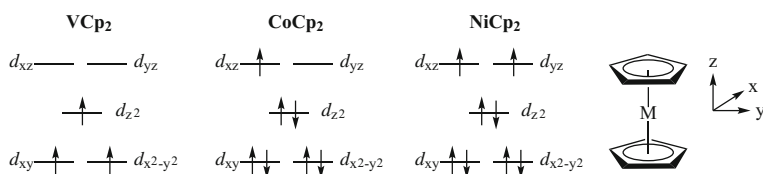


Fig. 5.18 Occupation of the d -orbitals in archetypal mononuclear metallocenes

nickelocene the unpaired electrons are located in the d_{xz} and d_{yz} orbitals (Fig. 5.18), which have sufficient overlap with the orbitals of the Cp ligands allowing a distribution of the spin density throughout the ligands and the aromatic linker [83–85]. In vanadocene the unpaired electrons occupy the d_{xy} , $d_{x^2-y^2}$ and d_{z^2} orbitals. Due to the missing overlap of these orbitals with the orbitals of the Cp ligands hardly any spin transfer occurs to the ligands or the aromatic linker and an exchange interaction is strongly reduced [84].

The clear distinction between intra- and intermolecular exchange interactions of bismetallocenyl complexes is challenging considering the crystal packing in the solid state. For the decamethyl bisnickelocenyl complex $[\text{Ni}^*]_2$ the molecules form chains in the crystalline state, resulting in similar inter- and intramolecular Ni–Ni distances (Fig. 5.19) [85]. The analysis of diamagnetically diluted samples as well as DFT calculations revealed that the magnetic behavior in the solid state of the naphthalene-bridged bismetallocenyl complexes is dominated by an intramolecular exchange interaction [83–85].

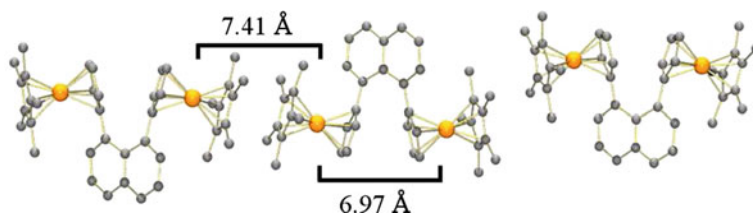


Fig. 5.19 Intra- versus intermolecular Ni–Ni distance in the crystal packing of $[\text{Ni}^*]_2$ [85]

5.4.2 More Stacking

The increase of the number of stacked metallocenes in a spin chain might also have a strong influence on the intramolecular exchange interactions. Therefore, the naphthalene-bridged tri- and tetranuclear cobaltocenyl complexes served as model compounds, bearing three and four $S = 1/2$ spin centers, respectively.

Synthesis

In order to increase the number of naphthalene-bridged cobaltocenes stacked in one direction, the asymmetrically functionalized key compound **2** was synthesized using 1,8-diiodonaphthalene (**1**) as starting material. It was then subjected to a mono iodine-lithium exchange reaction followed by a nucleophilic attack of the in situ formed lithium organyl at cobaltocenium iodide [92] (Scheme 5.8(i)).

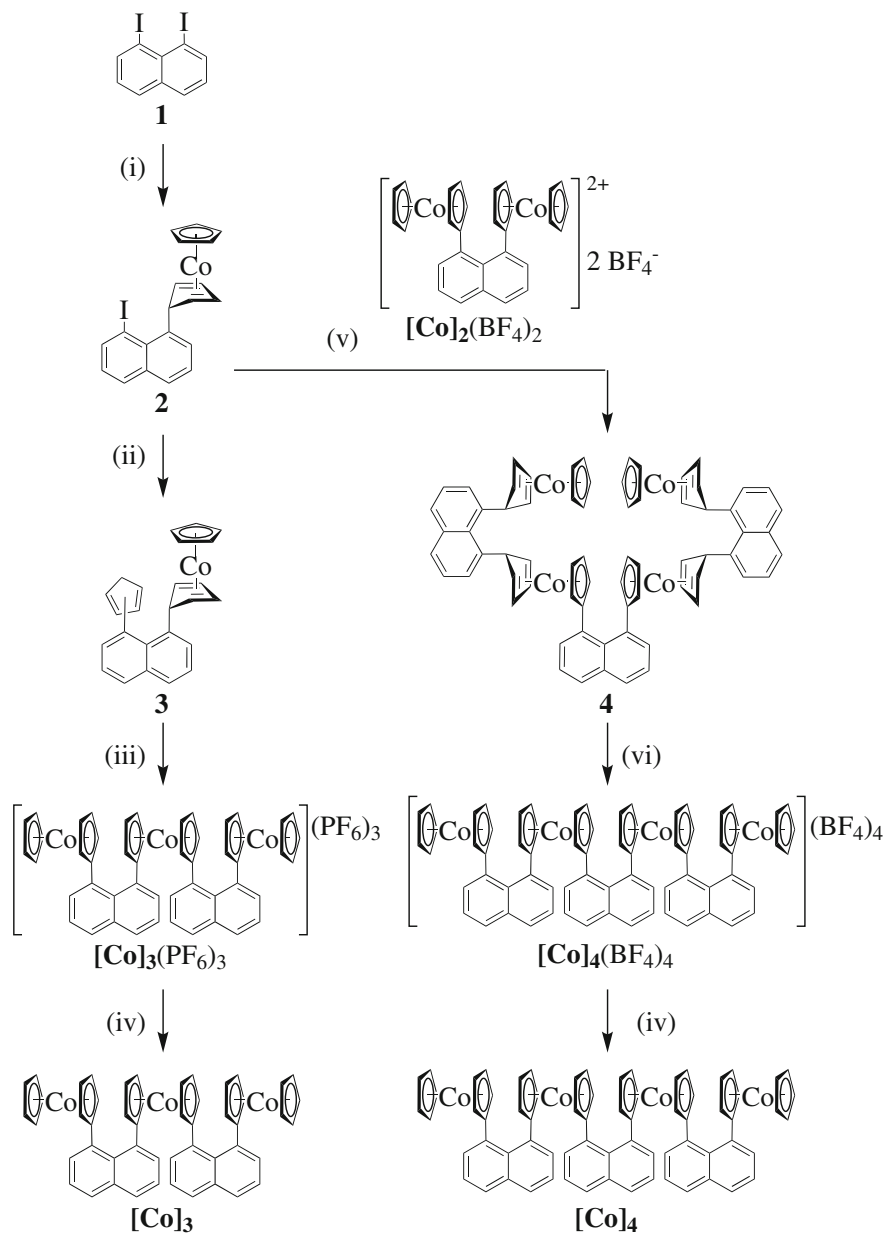
The remaining iodo substituent was replaced with a cyclopentadiene substituent in a cross coupling reaction with cyclopentadienyl zinc chloride in the presence of copper(I) iodide. The resulting mixture of **3** was transferred to the cationic trinuclear cobaltocenium complex $[\text{Co}]_3(\text{PF}_6)_3$ by deprotonation of the CpH substituent and addition of cobalt(II) chloride.

The oxidation of the formed cobaltocene complex was followed by a two-fold hydride abstraction. Finally, the reduction with decamethylcobaltocene yields the trinuclear air- and moisture sensitive target compound $[\text{Co}]_3$ [92] (Scheme 5.8(ii), (iv)).

In order to synthesize the tetranuclear cobaltocene complex, the key compound **2** was transferred into a nucleophile via an iodine-lithium exchange and was allowed to attack the biscobaltocenium complex $[\text{Co}]_2(\text{BF}_4)_2$ leading to the tetranuclear cobalt(I) complex **4**. A four-fold hydride abstraction yields the tetranuclear cobaltocenium complex $[\text{Co}]_4(\text{BF}_4)_4$, which can be reduced to the desired air- and moisture sensitive tetranuclear cobaltocene complex $[\text{Co}]_4$ using decamethylcobaltocene (Scheme 5.8(v)).

Molecular Structures

X-ray crystal structure determination revealed small structural variations of the stacked cobaltocenium complexes with increasing number of stacked cobaltocenium moieties $[\text{Co}]_2(\text{BF}_4)_2$ [86], $[\text{Co}]_3(\text{PF}_6)_3$ and $[\text{Co}]_4(\text{BF}_4)_4$ (Fig. 5.20). The distance between cobalt atoms in close proximity varies between 6.37 Å in $[\text{Co}]_3(\text{PF}_6)_3$ and



Scheme 5.8 Synthesis of the tri- and tetranuclear cobaltocenyl complexes $[\text{Co}_3]$ [92] and $[\text{Co}_4]$; reaction conditions: (i): (1) *n*-BuLi, Et₂O, (2) $[\text{CoCp}_2]$, Et₂O; (ii): CpZnCl, CuI, thf; (iii): (1) *n*-BuLi, thf, (2) CoCl₂, thf, (3) H₂O, NH₄PF₆, O₂, (4) Ph₃C⁺PF₆⁻, dem; (iv): CoCp₂^{*}, thf; (v): (1) *n*-BuLi, thf, (2) $[\text{Co}_2(\text{BF}_4)_2]$; (vi): Ph₃C⁺BF₄⁻

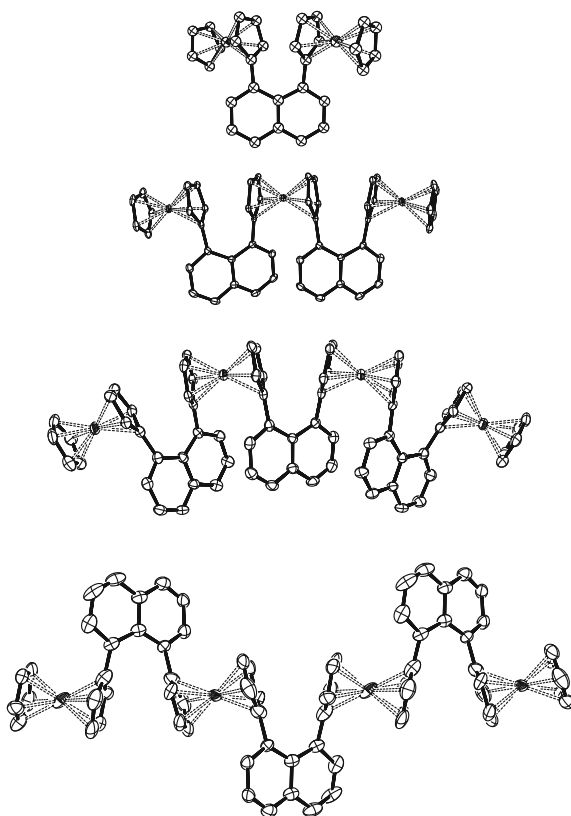


Fig. 5.20 Molecular structures of $[\text{Co}]_2(\text{BF}_4)_2$ (Co1–Co2 6.38 Å) [86], $[\text{Co}]_3(\text{PF}_6)_3$ (Co1–Co2 6.37 Å, Co1–Co3 12.72 Å), $[\text{Co}]_4(\text{BF}_4)_4$ (Co1–Co2 6.44 Å, Co1–Co3 12.66 Å, Co1–Co4 18.39 Å) and $[\text{Co}]_4(\text{BPh}_4)_4$ (Co1–Co2 6.7 Å, Co1–Co3 13.41 Å, Co1–Co4 20.11 Å); hydrogen atoms, counterions and co-crystallized solvent molecules are omitted for clarity

6.44 Å in $[\text{Co}]_4(\text{BF}_4)_4$. The Co1–Co3 distance of 12.72 Å in $[\text{Co}]_3(\text{PF}_6)_3$ drops to 12.66 Å in $[\text{Co}]_4(\text{BF}_4)_4$. The remarkable bent structure of $[\text{Co}]_4(\text{BF}_4)_4$ is attributed to the fact that the three naphthalene linkers are placed on the same side of the cobaltocenium chain. An X-ray crystal structure analysis of the tetranuclear cobaltocenium complex with a different counterion $[\text{Co}]_4(\text{BPh}_4)_4$ revealed an alternating placement of the naphthalene linkers with an increased Co1–Co2 distance of 6.70 Å (Fig. 5.20). Correspondingly, the distance of the outer cobalt atoms Co1–Co4 (20.11 Å) is increased compared to the value in $[\text{Co}]_4(\text{BF}_4)_4$ (18.39 Å).

Redox Properties

The redox properties of the di-, tri- and tetranuclear cobaltocenyl complexes were studied by means of square wave voltammetry (SWV). The measurements of $[\text{Co}]_2(\text{BF}_4)_2$, $[\text{Co}]_3(\text{PF}_6)_3$ and $[\text{Co}]_4(\text{BF}_4)_4$ revealed two, three and four separated,

Fig. 5.21 SWV of $[\text{Co}]_2(\text{BF}_4)_2$, $[\text{Co}]_3(\text{PF}_6)_3$ and $[\text{Co}]_4(\text{BF}_4)_4$ (top to bottom); MeCN, RT, $[\text{nBu}_4\text{N}][\text{B}(\text{C}_6\text{F}_5)_4]$ (0.1 M), versus Fc/Fc⁺, $\nu = 100 \text{ mV/s}$

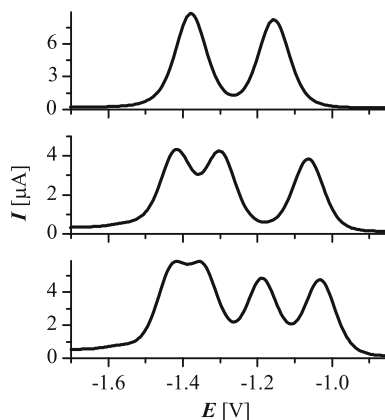


Table 5.6 SVW data of $[\text{Co}]_2(\text{BF}_4)_2$, $[\text{Co}]_3(\text{PF}_6)_3$ and $[\text{Co}]_4(\text{BF}_4)_4$

	$[\text{Co}]_2(\text{BF}_4)_2$	$[\text{Co}]_3(\text{PF}_6)_3$	$[\text{Co}]_4(\text{BF}_4)_4$
$E_{1/2}$ (1)	-1.160	-1.064	-1.044
$E_{1/2}$ (2)	-1.382	-1.296	-1.195
$E_{1/2}$ (3)		-1.419	-1.342
$E_{1/2}$ (4)			-1.430
$\Delta E_{1/2}$ (1/2); (K_c)	0.222 (5.65×10^3)	0.232 (8.35×10^3)	0.151 (3.57×10^2)
$\Delta E_{1/2}$ (2/3); (K_c)		0.123 (1.20×10^2)	0.171 (7.77×10^2)
$\Delta E_{1/2}$ (3/4); (K_c)			0.050 (7.00)
$\Delta E_{p/2}$ (1)	0.102	0.105	0.116
$\Delta E_{p/2}$ (2)	0.101	0.099	0.104
$\Delta E_{p/2}$ (3)		0.113	0.097
$\Delta E_{p/2}$ (4)			0.103
$\Delta E_{p/2}$ (Fc/Fc ⁺)	0.104	0.102	0.110

MeCN, RT, $[\text{nBu}_4\text{N}][\text{B}(\text{C}_6\text{F}_5)_4]$ (0.1 M), working electrode: Pt-disk, counter electrode: Pt-rod, reference electrode: Pt-wire, versus Fc/Fc⁺, $\nu = 100 \text{ mV/s}$, frequency 10 Hz, step potential 5 mV, potentials in (V) $\pm 0.005 \text{ V}$, $K_c = \exp(nF\Delta E_{1/2}/(RT))$

reversible redox events (Fig. 5.21) in the typical range of the cobaltocene/cobaltocenium redox couple [93] (Table 5.6), indicating electronic communication between the cobalt centers [92].

Magnetic Behavior

The magnetic behavior of the di-, tri- and tetranuclear cobaltocene complexes in solution was studied by ¹H NMR spectroscopy at variable temperature (Fig. 5.22). $[\text{Co}]_2$ [83], $[\text{Co}]_3$ and $[\text{Co}]_4$ revealed a linear correlation between the experimental chemical shift and the reciprocal temperature in the observed temperature range according to (5.1) [94].

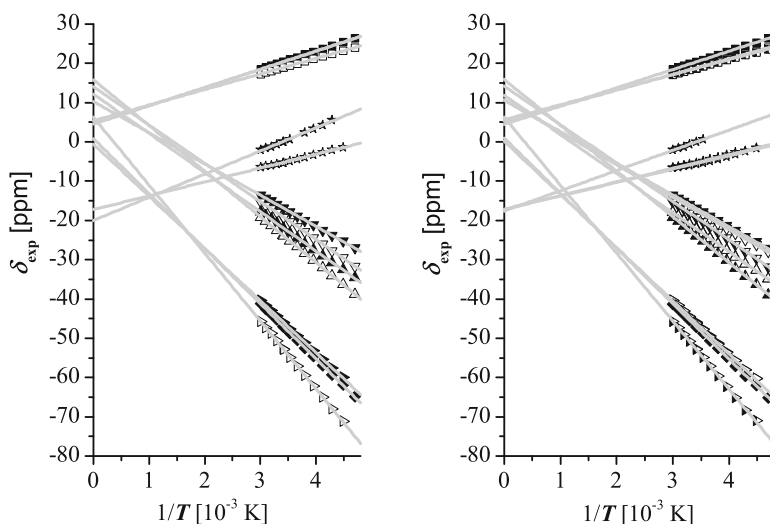


Fig. 5.22 Curie plot of the ^1H NMR measurements of $[\text{Co}]_3$ $R^2 = 0.994\text{--}1.000$ (left) and $[\text{Co}]_4$ $R^2 = 0.984\text{--}0.999$ (right); toluene- d_8 , 400 MHz (213–333 K)

$$\delta_{\text{exp}} = \frac{Ag_e\mu_B S(S+1)}{3\frac{\gamma_{\text{H}}}{2\pi}k_B T} + \delta_{\text{dia}}$$

A : hyperfine coupling constant,
 γ_{H} : gyromagnetic ratio of the proton

(5.1)

The unusual intercepts, representing the diamagnetic shift δ_{dia} , might be attributed to the cobaltocene anomaly [94] or even to a small intramolecular exchange interaction between the spins, which cannot be simulated for the spin systems due to the small temperature range of measurement.

In the solid state the magnetic susceptibility of $[\text{Co}]_3$ and $[\text{Co}]_4$ was measured by a vibrating sample magnetometer (VSM) between 3 and 300 K. For both complexes the temperature dependence of the effective magnetic moment indicate an antiferromagnetic exchange interaction (Fig. 5.23).

For both complexes the temperature dependence of the effective magnetic moment indicate an antiferromagnetic exchange interaction

The magnetic data of the trinuclear complex could neither be simulated for a simple $S_1 = S_2 = S_3 = 1/2$ spin system with $g_1 = g_3$ nor treated as a Heisenberg chain, indicating a more complex intermolecular exchange interaction. In the case of the tetranuclear complex, the data can be satisfactorily fitted [69] for a $S_1 = S_2 = S_3 = S_4 = 1/2$ spin system with $g_1 = g_4$ and $g_2 = g_3$ under the assumption that there is only an antiferromagnetic exchange interaction between adjacent spin centers (Fig. 5.24).

The exchange interactions obtained from the fit indicate an increased intramolecular coupling of -58.7 and -103.2 cm^{-1} (Table 5.7) compared to the dinuclear com-

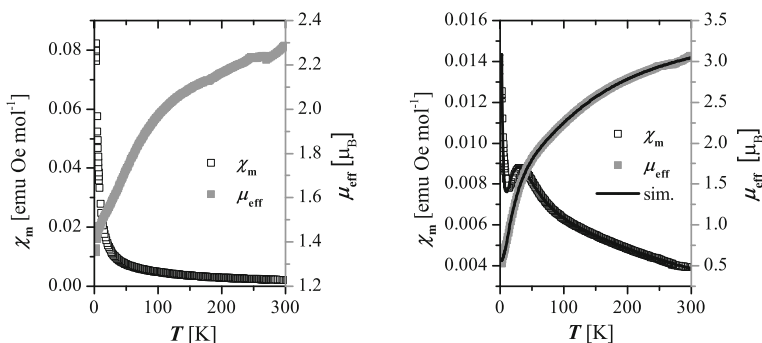


Fig. 5.23 VSM measurements of $[\text{Co}]_3$ (left) and $[\text{Co}]_4$ (right) in the solid state (field-cooled, 1 T)

Fig. 5.24 The spin system of $[\text{Co}]_4$

$$S_1 = S_2 = S_3 = S_4 = 1/2$$

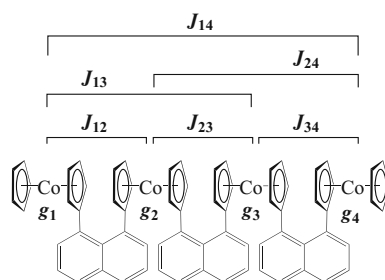


Table 5.7 Parameters obtained from fitting [69] of the magnetic data of $[\text{Co}]_4$ in the solid state

$g_1 = g_4$	$g_2 = g_3$	$J_{12} = J_{34}$ (cm^{-1})	J_{23} (cm^{-1})	Θ_{W} (K)	μ_{eff} (μ_{B}) (300 K)
2.002	2.34	-58.7	-103.2	-11.6	3.04, 3.46 [†]

[†]Expected value for a non-interacting $S_1 = S_2 = S_3 = S_4 = 1/2$ spin system according to the spin-only formula [9]

pound $[\text{Co}]_2$ (-28.1 cm^{-1}). The antiferromagnetic exchange interaction was also confirmed by DFT calculations [88]. Since no exchange interaction for the isolated molecules in solution was observed, it is likely that the increased antiferromagnetic coupling is influenced by intermolecular interaction in the solid state.

Molecules on Surfaces

The di- and trinuclear complexes can be successfully deposited on surfaces by using the air- and moisture stable related cobaltocenium complexes [92] (Fig. 5.25). The identification of the oligonuclear complexes on the surface is, however, challenging considering that different conformers are possible. This is best illustrated for the molecular structure of the corresponding cobaltocenium complex of $[\text{Co}]_4$ (Fig. 5.20).

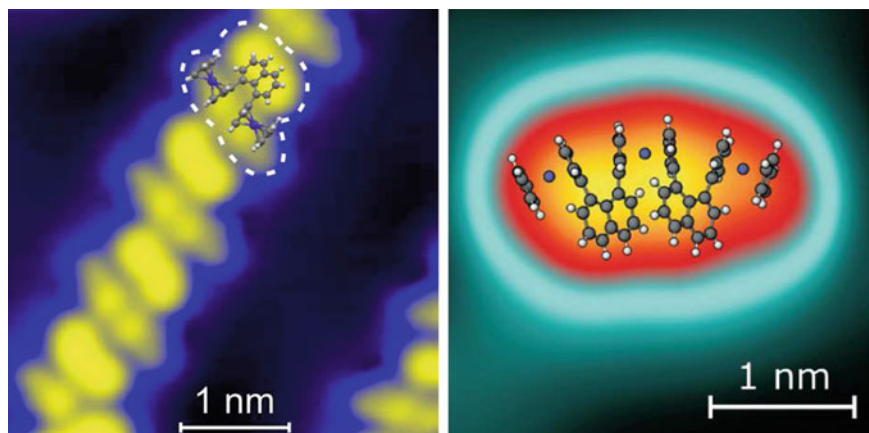


Fig. 5.25 Scanning tunnelling microscope images of $[\text{Co}]_2$ on a Au(111) surface (left) and $[\text{Co}]_3$ on a Cu(111) surface

References

1. S.J. Blundell, *Lect. Notes Phys.* **697**, 345 (2006)
2. O. Kahn, *Molecular Magnetism* (Wiley-VCH, Weinheim, 1993)
3. A.N. Holden, B.T. Matthias, P.W. Anderson, H.W. Lewis, *Phys. Rev.* **102**, 1463 (1956)
4. S. Ferlay, T. Mallah, L. Ouahes, P. Veillet, M. Verdagner, *Nature* **378**, 701 (1995)
5. S.D. Holmes, G.S. Girolami, *J. Am. Chem. Soc.* **121**, 5593 (1999)
6. S. Blundell, *Magnetism in Condensed Matter* (Oxford University Press, Oxford, 2001)
7. P. Gütlich, Y. Garcia, H.A. Goodwin, *Chem. Soc. Rev.* **29**, 419 (2000)
8. S. Chittipeddi, K.R. Cromack, J.S. Miller, A.J. Epstein, *Phys. Rev. Lett.* **58**, 2695 (1987)
9. J.S. Miller, A.J. Epstein, *Angew. Chem. Int. Ed. Engl.* **33**, 385 (1994)
10. J.S. Miller, *Inorg. Chem.* **39**, 4392 (2000)
11. T. Lis, *Acta Crystallogr. Sect. B* **36**, 2042 (1980)
12. R. Sessoli, D. Gatteschi, A. Caneschi, M.A. Novak, *Nature* **365**, 141 (1993)
13. R. Sessoli, H.L. Tsai, A.R. Schake, S. Wang, J.B. Vincent, K. Folting, D. Gatteschi, G. Christou, D.N. Hendrickson, *J. Am. Chem. Soc.* **115**, 1804 (1993)
14. A. Caneschi, D. Gatteschi, N. Lalioti, C. Sangregorio, R. Sessoli, G. Venturi, A. Vindigni, A. Rettori, M.G. Pini, M.A. Novak, *Angew. Chem.* **113**, 1810 (2001)
15. R. Clérac, H. Miyasaka, M. Yamashita, C. Coulon, *J. Am. Chem. Soc.* **124**, 12837 (2002)
16. J.S. Miller, M. Drillon, *Magnetism: Molecules to Materials* (Wiley-VCH, Weinheim, 2001)
17. S. Altmannshofer, E. Herdtweck, F.H. Köhler, R. Miller, R. Mölle, E.W. Scheidt, W. Scherer, C. Train, *Chem. Eur. J.* **14**, 8013 (2008)
18. E. König, V.P. Desai, B. Kanellakopulos, F.H. Köhler, *Chem. Phys.* **80**, 263 (1983)
19. H. Hilbig, P. Hudeczek, F.H. Köhler, X. Xie, P. Bergerat, O. Kahn, *Inorg. Chem.* **37**, 4246 (1998)
20. P. Hudeczek, F.H. Köhler, *Organometallics* **11**, 1773 (1992)
21. G.E. McManis, R.M. Nielson, M.J. Weaver, *Inorg. Chem.* **27**, 1827 (1988)
22. S.C. Jones, S. Barlow, D. O'Hare, *Chem. Eur. J.* **11**, 4473 (2005)
23. G. Laus, C.E. Strasser, M. Holzer, K. Wurst, G. Puerstinger, K.H. Ongania, M. Rauch, G. Bonn, H. Schottenberger, *Organometallics* **24**, 6085 (2005)
24. C. Elschenbroich, M. Wolf, O. Schiemann, K. Harms, O. Burghaus, J. Pebler, *Organometallics* **21**, 5810 (2002)

25. M. Rosenblum, H.M. Nugent, K.S. Jang, M.M. Labs, W. Cahalane, P. Klemarczyk, W.M. Reiff, *Macromolecules* **28**, 6330 (1995)
26. C. Elschenbroich, B. Kanellakopoulos, F.H. Köhler, B. Metz, R. Lescouëzec, N.W. Mitzel, W. Strauß, *Chem. Eur. J.* **13**, 1191 (2007)
27. H. Hopf, J. Dannheim, *Angew. Chem.* **100**, 724 (1988)
28. R. Roers, F. Rominger, B. Nuber, R. Gleiter, *Organometallics* **19**, 1578 (2000)
29. C. Schaefer, G. Scholz, R. Gleiter, T. Oeser, F. Rominger, *Eur. J. Inorg. Chem.* 1274–1281 (2005)
30. A.A. Khajetoorians, J. Wiebe, B. Chilian, R. Wiesendanger, *Science* **332**, 1062 (2011)
31. R.A. Layfield, *Organometallics* **33**(5), 1084 (2014)
32. J.R. Friedman, M.P. Sarachik, *Annu. Rev. Condens. Matter Phys.* **1**(1), 109 (2010)
33. L. Bogani, W. Wernsdorfer, *Nat. Mater.* **7**, 179 (2008)
34. A.A. Khajetoorians, J. Wiebe, B. Chilian, R. Wiesendanger, *Science (New York, N.Y.)* **332**(6033), 1062 (2011)
35. S. Kuck, S.H. Chang, J.P. Klöckner, M.H. Prosenc, G. Hoffmann, R. Wiesendanger, *ChemPhysChem* **10**, 2008 (2009)
36. S. Fremy, A. Schwarz, K. Lämmle, M.H. Prosenc, R. Wiesendanger, *Nanotechnology* **20**, 405608 (2009)
37. A. DiLullo, S.H. Chang, N. Baadji, K. Clark, J.P. Klöckner, M.H. Prosenc, S. Sanvito, R. Wiesendanger, G. Hoffmann, S.W. Hla, *Nano Lett.* **12**, 3174 (2012)
38. E. Sierda, M. Abadia, J. Brede, M. Elsebach, B.E.C. Bugenhagen, M.H. Prosenc, C. Rogero, M. Bazarnik, R. Wiesendanger, *ACS Nano* **11**, 9200 (2017)
39. B.E.C. Bugenhagen, M.H. Prosenc, *Dalton Trans.* **45**, 7460 (2016)
40. B.E.C. Bugenhagen, M.H. Prosenc (Manuscript in preparation)
41. M. Bazarnik, B. Bugenhagen, M. Elsebach, E. Sierda, A. Frank, M.H. Prosenc, R. Wiesendanger, *Nano Lett.* **16**(1), 577 (2016)
42. C. Garcia-Fernandez, E. Sierda, M. Abadia, B.E.C. Bugenhagen, M.H. Prosenc, R. Wiesendanger, M. Bazarnik, J.E. Ortega, J. Brede, E. Matito, A. Arnau, *J. Phys. Chem. C* (submitted)
43. J. Oldengott, A. Stammler, H. Bögge, T. Glaser, *Dalton Trans.* **44**, 9732 (2015)
44. P.H.M. Budzelaar, *Eur. J. Inorg. Chem.* **2012**(3), 530 (2012)
45. S.K. Russell, A.C. Bowman, E. Lobkovsky, K. Wieghardt, P.J. Chirik, *Eur. J. Inorg. Chem.* **2012**(3), 535 (2012)
46. S.C.E. Stieber, C. Milsmann, J.M. Hoyt, Z.R. Turner, K.D. Finkelstein, K. Wieghardt, S. DeBeer, P.J. Chirik, *Inorg. Chem.* **51**(6), 3770 (2012)
47. D. Sieh, M. Schlimm, L. Andernach, F. Angersbach, S. Nüchel, J. Schöffel, N. Šušnjar, P. Burger, *Eur. J. Inorg. Chem.* **2012**(3), 444 (2012)
48. S.C. Bart, K. Chlopek, E. Bill, M.W. Bouwkamp, E. Lobkovsky, F. Neese, K. Wieghardt, P.J. Chirik, *J. Am. Chem. Soc.* **128**(42), 13901 (2006)
49. T. Buban, Untersuchungen zu abstandsabhängigen magnetischen Wechselwirkungen in schwach gekoppelten Mehrkernsystemen. Dissertation, Universität Hamburg, Hamburg, 2017
50. N. Miyaoura, A. Suzuki, *Chem. Rev.* **95**(7), 2457 (1995)
51. W. Dammann, T. Buban, C. Schiller, P. Burger, *Dalton Trans.* in press <http://pubs.rsc.org/en/content/articlepdf/2018/DT/C8DT02347F>
52. J. Cámpora, A.M. Naz, P. Palma, A. Rodríguez-Delgado, E. Álvarez, I. Tritto, L. Boggioni, *Eur. J. Inorg. Chem.* **2008**(11), 1871 (2008)
53. E.A.H. Griffiths, G.J.P. Britovsek, V.C. Gibson, I.R. Gould, *Chem. Commun.* **1999**(14), 1333 (1999)
54. B.L. Small, M. Brookhart, A.M.A. Bennett, *J. Am. Chem. Soc.* **120**(16), 4049 (1998)
55. Y. Huang, J. Chen, L. Chi, C. Wei, Z. Zhang, Z. Li, A. Li, L. Zhang, *J. Appl. Polym. Sci.* **112**(3), 1486 (2009)
56. R.-Q. Fan, D.-S. Zhu, L. Mu, G.-H. Li, Q. Su, J.-G. Ni, S.-H. Feng, *Chem. Res. Chin. Univ.* **21**(4), 496 (2005)
57. R.-Q. Fan, Y.-L. Yang, Z.-W. Lü, *Chem. Res. Chin. Univ.* **24**(1), 4 (2008)
58. Q. Knijnenburg, S. Gambarotta, P.H.M. Budzelaar, *Dalton Trans.* **2006**(46), 5442 (2006)

59. F.H. Allen, O. Kennard, D.G. Watson, L. Brammer, A.G. Orpen, R. Taylor, *J. Chem. Soc. Perkin Trans.* **2**(12), S1 (1987)
60. B.L. Small, M. Brookhart, *J. Am. Chem. Soc.* **120**(28), 7143 (1998)
61. T.M. Baker, T.L. Mako, A. Vasilopoulos, B. Li, J.A. Byers, M.L. Neidig, *Organometallics* **35**(21), 3692 (2016)
62. G.J.P. Britovsek., K. Clentsmith, V.C. Gibson, D.M.L. Goodgame, S.J. McTavish, Q.A. Pankhurst, *Catal. Commun.* **3**(5), 207 (2002)
63. P. Gütllich, *Mössbauer spectroscopy and transition metal chemistry* (2011)
64. Y. Yoshida, G. Langouche, *Mössbauer Spectroscopy* (Springer, Berlin, 2013)
65. P. Gütllich, *Chem. unserer Zeit* **4**(5), 133 (1970)
66. N.N. Greenwood, T.C. Gibb, *Mössbauer Spectroscopy* (Springer, Netherlands, Dordrecht, 1971)
67. T. Buban, P. Burger (Manuscript in preparation)
68. A.A. Granovsky, T. Buban, P. Burger, Manuscript in preparation. (FireFly version 8, <http://classic.chem.msu.su/gran/firefly/index.html>)
69. E. Bill, *JulX simulation of molecular magnetic data* (2008)
70. E. Evangelio, D. Ruiz-Molina, *Eur. J. Inorg. Chem.* **2005**(15), 2957 (2005)
71. A.S. Attia, O.-S. Junga, C.G. Pierpont, *Inorg. Chim. Acta* **226**(1), 91 (1994)
72. C.G. Pierpont, *Coord. Chem. Rev.* **216–217**, 99 (2001)
73. N. Shaikh, S. Goswami, A. Panja, X.-Y. Wang, S. Gao, R.J. Butcher, P. Banerjee, *Inorg. Chem.* **43**(19), 5908 (2004)
74. A. Gerli, K.S. Hagen, L.G. Marzilli, *Inorg. Chem.* **30**(24), 4673 (1991)
75. C. Fukuhara, K. Tsuneyoshi, N. Matsumoto, S. Kida, M. Mikuriya, M. Mori, *J. Chem. Soc. Dalton Trans.* **1990**(11), 3473 (1990)
76. V. Kasempimolporn, H. Okawa, S. Kida, *Bull. Chem. Soc. Jpn.* **52**(7), 1928 (1979)
77. I. Nemeč, H. Liu, R. Herchel, Z. Xuequan, Z. Trávníček, *Synth. Met.* **215**, 158 (2016)
78. A. Hinaut, R. Pawlak, E. Meyer, T. Glatzel, Beilstein *J. Nanotechnol.* **6**, 1927 (2015)
79. O.V. Salata, *Curr. Nanosci.* **1**(1), 25 (2005)
80. M. Hermanowicz, Private communication (21.12.2016)
81. J.A.J. Burgess, L. Malavolti, V. Lanzilotto, M. Mannini, S. Yan, S. Ninova, F. Totti, S. Rolf-Pissarczyk, A. Cornia, R. Sessoli, S. Loth, **6**, 8216 EP (2015)
82. J. Tersoff, D.R. Hamann, *Phys. Rev. B* **31**(2), 805 (1985)
83. N. Pagels, O. Albrecht, D. Görlitz, A.Y. Rogachev, M.H. Prosenc, J. Heck, *Chem. Eur. J.* **17**, 4166 (2011)
84. S. Puhl, T. Steenbock, R. Harms, C. Herrmann, J. Heck, *Dalton Trans.* **46**, 15494 (2017)
85. S. Trtica, M.H. Prosenc, M. Schmidt, J. Heck, O. Albrecht, D. Görlitz, F. Reuter, E. Rentschler, *Inorg. Chem.* **49**, 1667 (2010)
86. N. Pagels, J. Heck, *J. Organomet. Chem.* **693**, 241 (2008)
87. K. Brandenburg, *Diamond*, Crystal Impact GbR, Bonn, version 3.1 edn. (1997–2005)
88. T. Steenbock, Understanding and controlling exchange spin coupling: insights from first-principles calculations. Ph.D. thesis, University of Hamburg, 2016
89. T. Steenbock, C. Herrmann, *J. Comput. Chem.* **39**, 81 (2018)
90. T. Steenbock, J. Tasche, A. Lichtenstein, C. Herrmann, *J. Chem. Theory Comput.* **11**, 5651 (2015)
91. L. Noodleman, *J. Chem. Phys.* **74**, 5737 (1981)
92. M. Gruber, T. Knaak, S. Puhl, F. Benner, A. Escibano, J. Heck, R. Berndt, *J. Phys. Chem. C.* **121**(48), 26777 (2017)
93. R.S. Stojanovic, A.M. Bond, *Anal. Chem.* **65**, 56 (1993)
94. I. Bertini, C. Luchinat, G. Parigi, *Solution NMR of Paramagnetic Molecules - Applications to Metallobiomolecules and Models* (Elsevier, New York, 2001)
95. F.H. Köhler, *J. Organomet. Chem.* **121**, C61 (1976)